DESIGN AND CONSTRUCTION OF A SILICON SCHOTTKY DIODE DETECTOR FOR SINGLE PROTON COUNTING AT THE MCMASTER MICROBEAM LABORATORY

BY:

TOMAS R. URLICH
B.Sc.

DESIGN AND CONSTRUCTION OF A SILICON SCHOTTKY DIODE DETECTOR FOR SINGLE PROTON COUNTING AT THE MCMASTER MICROBEAM LABORATORY

BY:

TOMAS R. URLICH, B.Sc.

A Thesis Submitted to the School of Graduate Studies in Partial Fulfillment of the Requirements for the Degree Master of Science

Master of Science (2017)	McMaster University
(Medical Physics)	Hamilton, Ontario

TITLE: Design and Construction of a Silicon Schottky Diode Detector for Single Proton Counting at the McMaster Microbeam Laboratory

AUTHOR: Tomas R. Urlich, B.Sc. (McMaster University)

SUPERVISORS: Jeroen Thompson & Soo Hyun Byun

NUMBER OF PAGES: ix, 42

Abstract

Microbeams have been used for radiation biology research since their introduction in the 1950s. A goal since their inception has been to irradiate individual cells and sub-cellular components with individual charged particles. These two criteria have been simultaneously achievable only within the last decade thanks to new technologies capable of producing very thin materials.

The McMaster Microbeam Laboratory wishes to conduct such experiments using a proton beam. However, there are presently no commercially available detectors for this application, which necessitates the need for a new detector. Following literature research, a 10 μm thin Schottky diode detector was selected as the most appropriate type of detector for the setup at McMaster. The design of the detector and detection system geometries were optimized to reduce beam scattering and broadening with the aid of TRIM and MCNP simulations.

Two detectors were fully constructed. However, a stable response to radiation was not achieved. One of the detectors appeared to function as a radiation detector very briefly but this result was not reproducible. The I-V curve of the detectors proved that they functioned as expected as diodes. However, without a radiation response no further characterization could be completed. Although problem solving efforts to overcome this issue were unsuccessful, a large silicon dopant concentration is suspected to be a possible cause.

Acknowledgements

When I began the medical physics program I was starting my journey in this field with much less background than the majority of my peers and I was very worried that I would be like a fish out of water. Luckily for me, there were many exceptional individuals that did not allow that to happen, to all of whom I express sincere gratitude. Your encouragement has assisted me more than you know.

I would like to thank my supervisors, Professor Jeroen Thompson and Professor Soo Hyun Byun for believing that a chemist could succeed in this program. Your mentorship and imparted wisdom will stay with me long into my career. I thank my committee members Professor Doug Boreham and Professor Bill Prestwich who have provided valuable suggestions, and Professor Fiona McNeill for finding a way to incorporate my hobbies into my academic career.

I thank Mr. Justin Bennett for providing unending technical support and answering more of my questions than anyone else, and Mr. Frank Labonte for his computer assistance. Mr. Shahram Tavakoli and Mr. Chris Butcher have aided greatly with my detector construction and Mr. Terry Wagg with machining new equipment. I must also thank Ms. Fiona Ahlang, Ms. Nancy Brand, Ms. Mary-Ellen Cybulski and Ms. Lisa Stoa for all of their administrative assistance.

I thank my family and friends for putting everything into perspective, especially my officemates in room 104B. Lastly, to those few who still think I'm a rocket scientist, thank you for inspiring me.

For my grandmother Wanda; *do następnego razu.*

Table of Contents

List of Figures

List of Tables

1. Introduction

1.1 Ion Beams

1.1.1 Microbeams

Microbeam accelerators are scientific instruments which accelerate a beam of charged particles, having a beam width in the micron to sub-micron scale. Thus, they have an ability to target and irradiate single cells and even individual components of a single cell, which has made them a valuable tool for radiation biology research. Irradiation of sub-cellular structures using proton microbeams was first implemented in the 1950s[1], In this case a Van de Graaff generator was used to accelerate 2 MeV protons through a microaperture. Since then the technology has expanded to beams composed of other charged particles including alpha particles and carbocations. Microbeam technologies have been continually improving in a number of other ways that has allowed them to stay relevant and important.

The goal for microbeams from their inception has been to be able to deliver a precise number of charged particles to as small of an area within a sample as possible[2]. This has proven to be the most challenging to achieve with proton beams for two fundamental reasons. First, the light mass of protons results in large scattering angles which complicates detection and constrains the geometry of all instrumentation involved in the experiments. In addition, proton beams have lower energies and lower ranges when compared to beams of other charged particles which limits sample and detector thicknesses[3]. Recently, these obstacles have been overcome with the development of new solid state detectors. The new detectors can measure the number of incident ions hitting a biological sample with improved accuracy. This greater irradiation control allows for the study of the effects of very low dose irradiations, down to the effects of a single charged particle. This is a research topic that has been of great interest for decades and now has finally enabled the study of the bystander effect in *in vivo* systems[4].

In the only related publication to date, researchers irradiated 35 μm spots on ears of sedated mice with a 3 MeV proton beam. The formation of γ-H2AX foci, a compound created when radiation triggered protein modification occurs, was compared between the irradiated and control ears of each mouse by immunohistochemical analysis of the epidermis. It was observed that the foci formed in an average of 20 cells around each of the directly irradiated cells which is direct evidence of the bystander effect. This result demonstrates the potential ability of this model to be used for further studies[4]. There is also precedent for other techniques such as capillary electrophoresis to be used in conjunction with microbeams to analyze chemical radicals formed during irradiation[5].

1.1.2 The McMaster Microbeam Laboratory

The McMaster Microbeam Laboratory was built using a 3 MV KN Van de Graaff accelerator capable of producing monoenergetic proton beams up to 3 MeV in energy and alpha particle beams up to 6 MeV. The laboratory is licensed to operate the accelerator with a beam current of up to 10 μm, which is measured on a Faraday cup situated where the beam exits the accelerator. The beam initially has a horizontal trajectory in a high vacuum chamber with a pressure typically between 1×10^{-7} and 1×10^{-6} Torr. The beam then reaches an analyzing magnet capable of bending it from a horizontal to vertical trajectory before terminating at an end-station located above in a Class 2 biological facility. At this stage the average pressure is 1×10^{-4} Torr.

The end station includes a Prior Scientific ProScan II X-Y stage and a Mad City Labs (MCL) nano-positioning XYZ stage for precise sample alignment. The MCL stage can be retrofitted to attach a customized mount. Microscopic imaging is achieved with a Nikon AZ100 Plan Fluor microscope. All important components of the McMaster Microbeam Laboratory are shown in Figure 1.1.

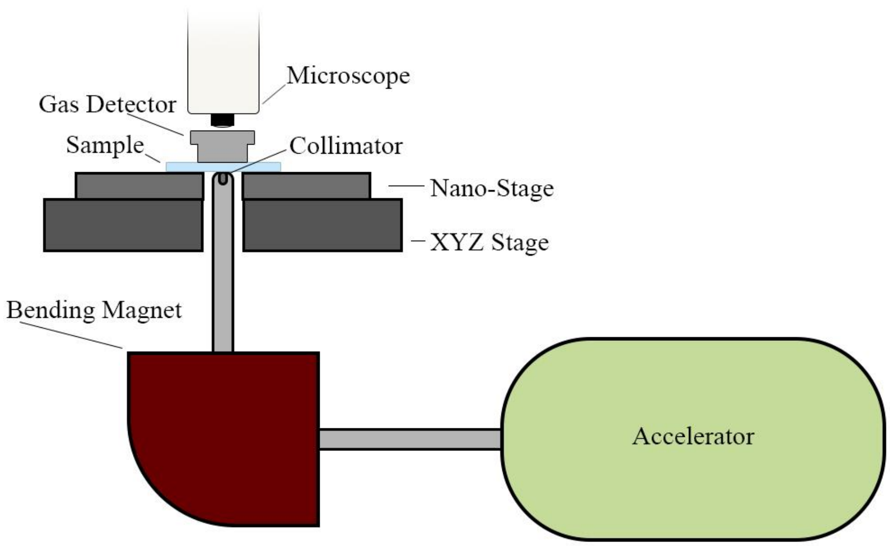

Figure 1.1: Simplified diagram of the McMaster Microbeam Laboratory. Sizes and distances are not to scale.

1.2 Solid State Detectors

1.2.1 Detector Physics

Semiconductor diode detectors, also referred to as solid state detectors, are a popular class of radiation detectors. They offer better energy resolution than scintillation detectors and are significantly smaller than gaseous proportional counters. In a given crystalline material, electrons that are in the outermost occupied valence shell of the crystal lattice are referred to as being in the valence band. The amount of energy required to liberate an electron from the valence band so that it can freely move within the crystal – within the so called conduction band – is the band gap energy. If the band gap is small then ambient thermal energy is enough to excite an electron across it. A crystalline material is categorized as a semiconductor when the band gap is small enough to be conductive. The vacancy left behind by the excited electron is called a hole, and together with the electron they are called an electron-hole pair[6].

1.2.2 Depletion Depth

When a bias is applied to a solid state detector via an electrode, an electric field is established. As the bias increases, the size of electric field also increases, extending away from the electrode. In the presence of an electric field, the electrons and holes move quickly in opposite directions towards the edge of the semiconductor where they can be collected. An electric field suppresses the amount of thermally generated electron-hole pairs which reduces detector noise. The semiconductor volume under the influence of this effect is called the depletion layer[6].

For both p-n and metal-semiconductor junctions, the depletion depths are inversely proportional to the square root of the impurity concentrations[7]. Since the range of possible impurity concentrations in silicon wafers is several orders of magnitude, it is important to calculate what bias voltage is required to achieve full depletion for a given concentration. To calculate the depletion depth of a metal-semiconductor junction, equations 1.1 through 1.4 can be used:

Equation 1.1: Depletion depth $$x_d = \sqrt{\frac{2\epsilon_r\epsilon_0(\phi_i - V_a)}{qN_d}}$$

Equation 1.2: Built-in potential $$\phi_i = \phi_B - kT\, ln\frac{N_v}{N_d}$$

Equation 1.3: Barrier height for P-type silicon $$\phi_B = \chi + \frac{E_g}{q} - \Phi_M$$

Equation 1.4: Barrier height for N-type silicon $$\phi_B = -\chi + \frac{E_g}{q} + \Phi_M$$

where ϵ_r is the dielectric constant (11.68 for Si), ϵ_0 is the permittivity of free space ($8.85 \times 10^{-12}\ F \cdot m^{-1}$), V_a is the applied negative voltage [V], q is the elementary charge, $8.85 \times 10^{-19}\ C$, N_d is the impurity concentration [$atoms \cdot cm^{-3}$], kT is the product of the Boltzmann constant and temperature (0.0259 eV at 300K), N_v is the density of valence band states ($1.83 \times 10^{19}\ cm^{-3}$ for Si), χ is the electron affinity (4.05 eV for Si), E_g is the band gap energy (1.12 eV at 300K Si) and Φ_M is the work function (4.8 eV for a Si-Au junction)[7].

1.2.3 Application to Microbeams

The method of determining the dose and dose rates experienced by irradiated cells largely determines how small of a dose can be accurately and reliably measured. Early light ion (proton, alpha) microbeam end stations placed their biological specimens between the end of the beam line (vacuum-air barrier) and their radiation detectors. The samples used in this setup had to be very thin so that each charged particle would have enough remaining energy to reach and register on the detector. Even if the sample had a low stopping power, the sample still needed to be thin to reduce beam scatter as a result of particle traversal through the sample[7]. In this arrangement, irradiation of more than a monolayer of cells is not ideal and any sort of *in vivo* measurements are impossible.

One technique developed to overcome this was the use of thin scintillation foils as detectors, placed in the path of the beam before the sample[8-10]. Detectors in this configuration are variably referred to as transmission and ΔE detectors, as well as pre-hit cell counters in the field of microbeam research. This technique allowed for accurate counting of protons. However, it had a significant shortcoming of requiring complete darkness during irradiation, which does not lend itself to being able to simultaneously image samples.

A new class of transmission detectors referred to as ultra-thin (< 50 microns thick) has the same advantages of the foil detectors while eliminating the requirement of darkness.[3] These ultra-thin transmission detectors are also placed in the path of the beam before the sample. Furthermore, they allow for more flexibility in sample type and sample preparation as thickness is no longer a limitation. However, there are currently no commercially available ultra-thin detectors, the closest being a 100 μm thick silicon detector in Ortec's D-series.[11] This necessitates the need to perform a comprehensive literature analysis of what other researchers have published, and to construct a detector for use in the McMaster Microbeam Laboratory.

A few research groups have begun to manufacture these types of detectors, each tailored for measurement of one type of charged particle with a particular range of energies. Most of the research has been conducted at Columbia University as well as by Lund University and their collaborators. Reported detectors have so far been fabricated based on both p-n junctions and metal-semiconductor junctions. The first designs that were described in literature were made from PIN silicon (three layers within the semi-conductor; p-type, intrinsic and n-type).[12-16]

The remaining designs are based on Schottky diodes, which are rectifying metal-semiconductor junctions.[3,17] These designs are simpler to build because they do not require semiconductor doping. In the only publication describing Schottky diode using silicon, detectors are based on a gold-silicon junction using 10 μm thin P-type silicon. A co-planar aluminum electrode is used for grounding. Due to the fragility of this assembly, it is mounted over a hole in a glass microscope slide for stability[17]. There is also only one publication describing the construction of a Schottky diode based on an aluminum-diamond junction[3]. In this case, a 6 μm synthetic semiconductor diamond membrane is used, with an aluminum grounding electrode in a sandwich configuration (Figure 1.2). Electronics grade diamond films grown by Chemical Vapour Deposition (CVD) are quite inexpensive, and their excellent structural integrity allows for diamond membrane transmission detectors to also function as the vacuum-air barrier at the end of a microbeam beamline[18].

Figure 1.2: Positioning of electrodes on Schottky diode transmission detectors in literature. Dimensions are not to scale.

Both types of detectors operate optimally with low biases of less than 50 V required to reach full depletion. Reported PIN detectors have been tested with silicon thicknesses of 4.15 – 26 microns and proton beam energies of 2.0 – 2.55 MeV. Silicon Schottky diode detectors have been tested with 8.5 – 13.5 micron silicon and 2.7 MeV protons. Diamond Schottky diode detectors have been tested with 6 micron diamond and 1.3 – 6.0 MeV protons.

Both designs have proven to have good performance for particle detection with a decent signal-to-noise ratio. The signal-to-noise ratio of the diamond detector in particular was found to be excellent at standard operating temperatures due to the negligibly low intrinsic noise of diamond. Radiation tolerance has been found to be quite high in thin silicon, and detectors are expected to last from months to years at particle fluences typical of microbeams[19]. Detector efficiency in each case was assessed by comparing the ratio of detection events between the transmission detector and a commercial silicon detector positioned in tandem. The range of efficiencies with proton beams were 70 – 99 % for various PIN detectors, and 99% for diamond Schottky diodes. Unfortunately, there is no direct comparison for the silicon Schottky diode detectors. The only efficiency measurement reported for them is >98% for 5.4 MeV alpha particles through an 8.5 μm detector.[17] The reported cause of detectors exhibiting lower efficiencies is a result of a poor pairing of proton energy and detector thickness. Linear energy transfer (LET) must carefully be considered when designing the detectors for specific applications as it will limit the range of detector thicknesses for useful operation. This suggests that although each individual detector is highly efficient within a small range of energies, multiple versions would be required to complete experiments at multiple beam energies. Other conclusions provided to explain differences in the detector efficiencies is not unanimous in the literature. For example, different reports by the same authors claim efficiency to be dependent on both bias voltage and beam energy[12] as well as dependent of bias voltage only[13].

It is pertinent to note that from all of the literature referenced above, no data is presented regarding the targeting abilities that each detector can afford when used with that facility's microbeam. In order to facilitate single cell targeting, the geometry of the entire beamline end station must be considered. This includes the non-active areas of the detector, and how the detector and sample are mounted.

1.3 A New Detector

1.3.1 Detector Requirements

The goal of this project was to design and construct a transmission detector suitable for 3 MeV proton beam irradiations. Additionally, once implemented, the detection system must allow for at least 95% of protons hitting the sample to do so within a radius of 20 μm. To this end, any beamline or end station modifications that would aid in achieving these goals were also possible components of the project. For scale, human cells are between 2 and 120 μm in length[20]. Collaborating biologists have chosen AGO1522 human fibroblasts as a candidate for study with microbeam irradiations. Human fibroblasts are shaped like a grossly elongated triangle. The effect of cell preparation on the shape of a similar cell line, AGO1523, has been studied in literature. The study measured cell lengths between 135.75 and 332.9 μm, and average cell widths between 20.64 and 47.04 μm[21]. The detector in this project would not be able to target individual cells if their average width lies in the lower end of this range. However, it will serve as the first generation of transmission detectors to be designed, constructed and used in irradiations, all in house.

1.3.2 Detector Type

Of the transmission detector types discussed in section 1.2.2, one needed to be chosen as the basis for detector construction. While there were the most examples of PIN silicon detectors in the literature to draw information from, the silicon doping process involves many steps including both high temperatures and toxic chemicals. Schottky diodes don't require silicon doping on both sides and so by comparison are a simpler and a greener alternative. A diamond membrane Schottky diode is the more attractive option. However, based on local expertise and equipment, the silicon based Schottky diode was chosen as the basis for detector construction.

1.3.3 Beam Collimation

To limit the beam width and solid angle at the irradiation target, all microbeams utilize either a focusing system or end-station collimation[22]. The McMaster Microbeam Laboratory has some beam focusing capabilities but it is insufficient for single cell targeting. The laboratory already possessed a set of double aperture collimators which were used as a starting point to assess how collimators affect beam shape. The geometry of an example double aperture collimator is shown in Figure 1.3. Based on the aperture diameter and total collimator length the relationship in Equation 1.5 can be used to find the maximum exit angle of the collimator. Using Equation 1.6 the corresponding solid angle can be found.

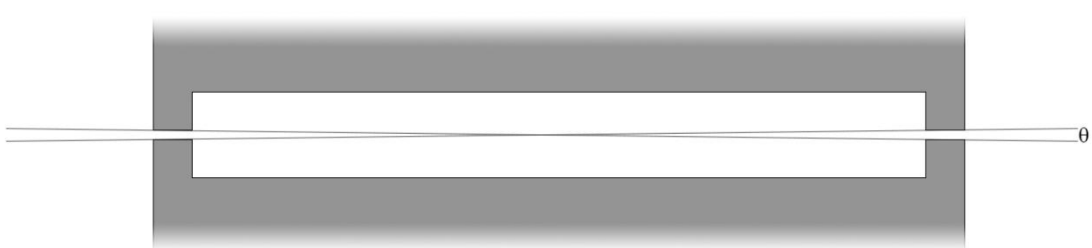

Figure 1.3: Double aperture collimator of 5 μm diameter apertures and a spacer length of 925 μm. Dimensions are to scale.

Equation 1.5: Exit angle θ $$tan\frac{\theta}{2} = \frac{aperture\ diameter}{collimator\ length}$$

Equation 1.6: Solid angle $$\Omega = 2\pi(1 - cos\theta)$$

Once the solid angles were found, beam broadening resulting exclusively from collimator geometry could be plotted as a function of distance from the collimators as shown in Figure 1.4. The beam broadens considerably in a very short distance for all of the collimators. Without even taking scattering or broadening due to repulsion into account, the goal of 95% of the beam within a 20 μm radius spot is not possible with these collimators and thus there was a need to design new ones. For reference, the collimator to target distance chosen in the following sections is 760 μm.

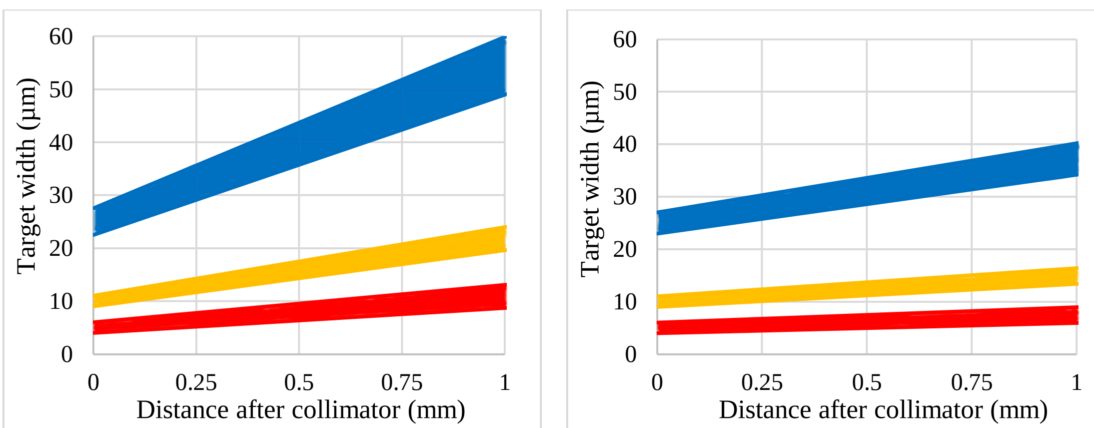

Figure 1.4: Target size due to collimation for existing (left) and new (right) double aperture collimators with aperture radii of 5±1 (red), 10±1 (yellow) and 25±2 (blue) microns.

The two parameters that would further decrease the solid angle coming out of the collimators are decreasing the aperture size and increasing the spacing between the two apertures. Of the existing collimators, the narrowest had a diameter of 5 ± 1 μm. This collimator had previously proven to be small enough to make beam alignment a tedious task. Further reduction in aperture size would be even more arduous and so 5 μm was again chosen as the narrowest aperture for a new collimator. Increasing the spacing between apertures was therefore the preferred modification. The plot in Figure 1.5 shows how the maximum angle of a proton leaving the collimator changes by increasing the aperture spacing.

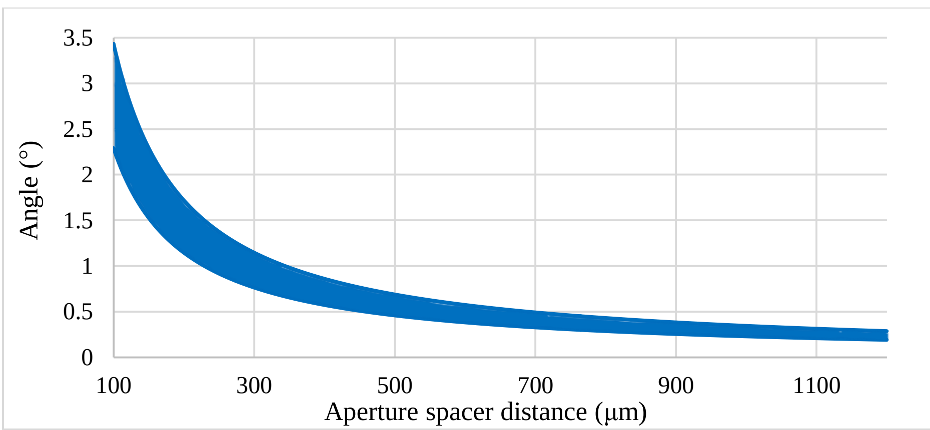

Figure 1.5: Maximum proton angle leaving a 5±1 micron diameter double aperture collimator.

A final criterion to consider when selecting parameters for new collimators is the fact that the narrower the beam exiting the collimator, the more beam is being attenuated by the collimator itself. The radiation biology experiments desired to be done at the McMaster Microbeam Laboratory do not require high proton fluences. To keep irradiation times short, proton rates as low as a single proton per second would be sufficient. However, it was still necessary to estimate the fluences after collimation. Without collimation, the beam current reaching the end of the beamline is approximately 5 pA or 3×10^7 protons/s. By taking the ratios of the known solid angle entering the collimator to those exiting the collimator, an estimate of the reduction in proton fluence can be made as shown in Figure 1.6. The plot shows that at all collimator geometries considered, the proton fluence remains at a level conducive to short irradiation times.

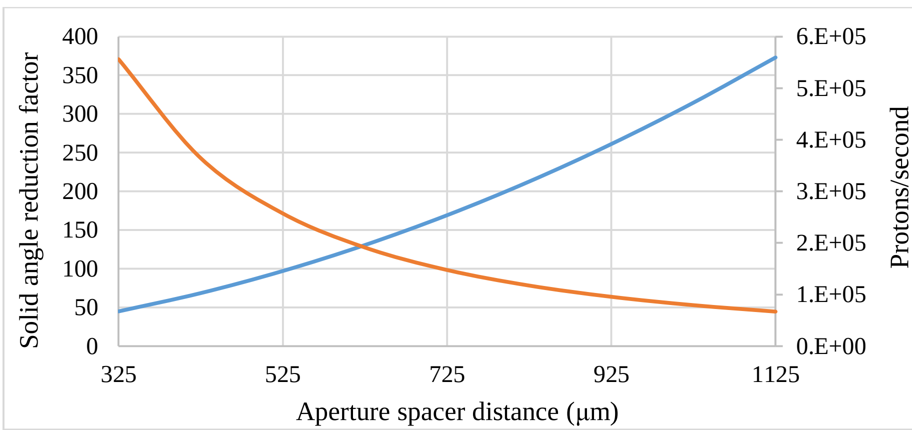

Figure 1.6: Proton fluence (orange) and beam solid angle reduction by the collimator (blue) as a function of collimator aperture spacer distance for a 5±1 μm diameter collimator.

1.3.4 Detector Thickness

The thickness of the detectors also requires some optimization. The detector must be thick enough so that sufficient proton energy is deposited to give a large enough signal that can reliably be counted as one passing proton. Conversely, the detector needs to be thin enough to keep beam scattering at a minimum and so that enough proton energy remains to be deposited in the sample. There are typically two type of interactions experienced by charged particles traversing a material, Rutherford scattering (elastic) and Coulombic interactions (inelastic). Since protons are both very light and small, Coulombic interactions are by far the predominant route of energy deposition and so stopping power alone can be used to estimate it. The plots in Figure 1.7 show both the stopping power and range of protons in silicon.

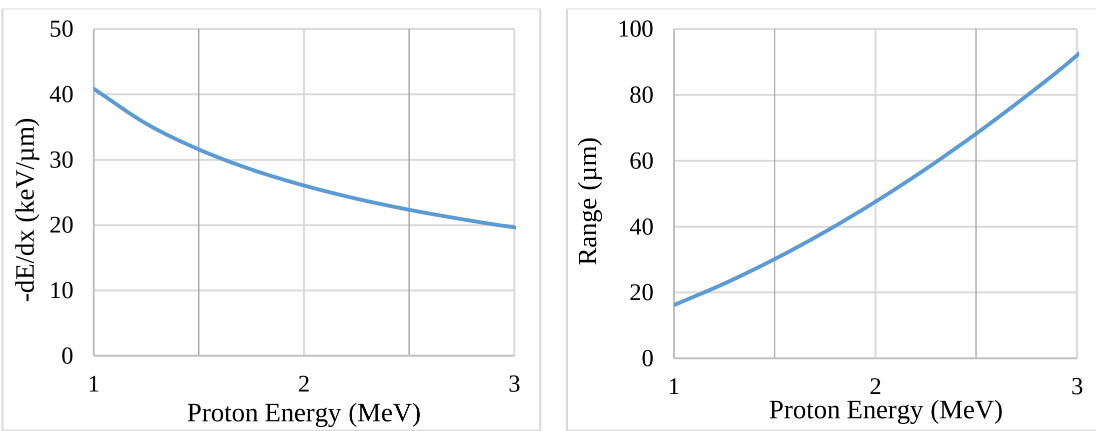

Figure 1.7: Stopping power (left) and range (right) of protons in silicon based on NIST data[23].

The only report of thin Schottky diodes used for proton beam detection found that for a 2.7 MeV beam, the most reliable counting statistics came from a 13.5 μm detector. The four detectors studied in that report ranged in thickness from 8.5 to 13.5 μm. As an initial parameter used in the design phase of the new detector, the detector thickness was 13.5 μm. Due to the commercial availability of ultra-thin silicon wafers at only one thickness (see section 2.1), 10 ± 2 μm silicon wafers were selected for incorporation into the detector.

1.3.5 Detector Geometry

The positioning of the detector and sample relative to where the proton beam passes through the vacuum-air barrier greatly affects what size of a spot will be irradiated on the sample. With the detector thickness already minimized, the vacuum-air barrier to sample distance must be reduced as much as possible to further minimize beam scattering and broadening. In particular, the detector and sample should be placed as close to each other as possible, since Rutherford scattering from beam interaction with the detector is much greater than scattering through air. A custom made mount to securely position the detector and sample was deemed a necessity and will be described in the section 2.6.

1.3.6 Silicon Wafers

Selecting the method for obtaining sufficiently thin silicon required careful consideration. Only one supplier of 10 ± 2 micron silicon, Virginia Semiconductor (Fredericksburg, USA) was found. However, at $1200 for four 1-inch diameter wafers it was worth searching for alternative methods. Furthermore, cleaving the wafers into detector-sized shapes without shattering would also pose a challenge due to the fact that at that thickness the wafers were flexible and extremely fragile. The other option was to purchase thicker wafers and thin them via mechanical grinding or plasma etching. Although these wafers would be significantly less expensive, both thinning methods would be incredibly difficult to achieve uniform thickness throughout the wafer, especially in the 10 micron range. Local experts advised that this would be impossible. Additionally, plasma etching requires equipment that was not conveniently accessible, while mechanical grinding is a very long, tedious and expensive process due to the large number and variety of specialty sand papers required per wafer. Ultimately, it was decided that since a low volume of detectors would be built, that purchasing the already thin wafers would save a significant amount of time and resources for process development.

1.3.7 Monte Carlo Simulations

The Monte Carlo method has been validated in literature as an accurate technique for modeling proton beams. With some algorithms, results are in excellent agreement when compared with measured values, and thus Monte Carlo simulations can be used to accurately model situations where measurement is difficult or impossible[24]. Transport of Ions in Motion (TRIM) is a very easy to use software package that can be used to simulate charged particle traversal through any given material[25]. Without any knowledge of coding, valuable information including ion energy loss and trajectory deviation can be obtained.

As great of an insight it is that TRIM provides, it does have its limitations. The source is limited to a monodirectional point source that can emit only one particle at a time. This is not a representative model for where a particle beam is involved. Additionally, geometry customization is constrained to only one dimension where only the thickness and elemental composition of each layer can be defined.

Monte Carlo N-Particle (MCNP) is another Monte Carlo method software package. Although there is a greater learning curve to use MCNP, it offers a much higher level of customization. In MCNP the geometry of all components of interest, even ones with complex shapes like the double aperture collimators, can be modeled. Because of this greater customization, MCNP would be the better choice in the context of detector design.

The F2 tally in MCNP computes average surface fluence over a given surface area. Adding the FS modifier to the tally subdivides the surface into any desired number of segments and computes the average surface fluence for each segment.

2. Methods & Materials

2.1 Silicon Wafers

The obtained 10 ± 2 μm thick wafers were cleaved in a clean room. Initially intended to be 0.9 cm squares, their thinness proved challenging to cleave. Each cleavage resulted in irregularly shaped fracture lines and shattered fragments. To reduce the total number of cleavages the circular wafers were cleaved into quarters rather than into squares.

2.2 Glass Preparation

To minimize the beam exit window to sample distance, thin glass was originally planned to be incorporated into the detector. Cover glass (VWR No. 2) with a rated thickness of 0.17 – 0.24 mm was acquired and measured to actually be 0.19 ± 0.01 mm. However, this cover glass proved too fragile to drill a hole through without shattering. Heating the glass allowed for a hole to be drilled. However, the excess glass beaded up on the edges of the hole rather than being expelled, which would not allow for proper adhesion to the silicon wafer and increased overall glass thickness. Additionally, the entire cover slide would warp during heating. Handling of this thickness of cover glass was tedious in general, one sample that was dropped only a few inches completely shattered. There was concern of the glass breaking at every stage of detector assembly and use so standard microscope slides (1mm thickness) were opted for instead. Using a dremmel at its highest speed, holes were drilled by using four diamond-tipped bits with successively larger diameters up to 6 mm. A small amount of water was applied to both sides of the glass before drilling to eliminate airborne glass dust. The edges of the holes were then sanded with a fine grit sandpaper.

2.3 Silicon Adhesion

The silicon wafers were adhered to the glass slides at the Canadian Centre for Electron Microscopy. Wafer-Mount 562, a thermoplastic adhesive film, was cut to roughly the size of wafer to be adhered and placed in position on top of the glass. This was then put on a hot plate, melting the adhesive. The silicon wafer was placed on top and after a few seconds the assembly was removed from the hot plate and then gently pressed together with spring-controlled press over the surface of the silicon. Any excess glue around the edges of the wafer was mostly removed by carefully dissolving it with a cotton swab dipped in acetone. This technique did not afford full removal of the excess adhesive. However, this is not expected to affect detector performance in any way.

2.4 Electrode Deposition

Gold and aluminum electrodes were deposited onto the detector at the Centre for Emerging Device Technologies. Both were deposited at a rate of 2.0 A/s up to a total thickness of 200 nm using a cover glass attached with kapton tape as a shadow mask. A small gap between the electrodes was left undeposited using a shadow mask.

The width of the gap was approximately 0.5 mm. Metal deposited on the glass outside the area of interest was removed by gentle scraping with a metal spatula.

2.5 Wire Attachment

Short wires were soldered to a female SHV connector, and another set of wires were adhered to the electrodes in the configuration in Figure 2.1 using a two component silver conductive epoxy (MG Chemicals) and cured overnight at room temperature. The same SHV head was used to attach all of the detectors constructed to the electronics by soldering and desoldering to the leads coming from each detector. The detector at each step of fabrication is shown in Figure 2.2.

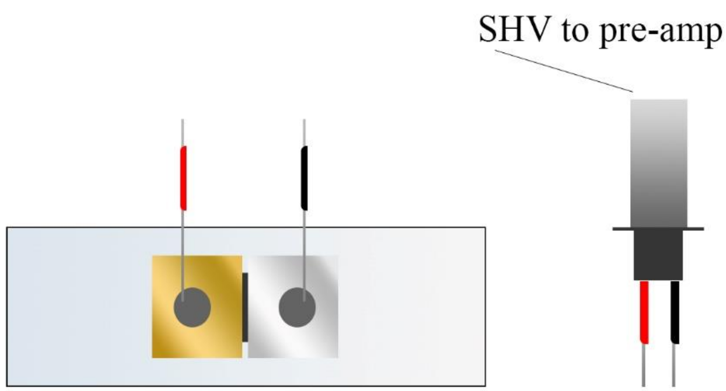

Figure 2.1: Detector wiring graphic. Dimensions are not to scale.

Figure 2.2: Transmission detector at each stage of construction.

2.6 Detector Mount

A custom mount plate for the thin detector was waterjet cut from aluminum and designed to attach to the existing microbeam end station (Figure 2.3). The mount is designed to screw into the MDL nano-positioning stage, to replace the existing mount for the existing gas flow proportional counter. The new mount has a slot to securely position the bottom of the detector in the same horizontal plane as the vacuum-air barrier (Figure 2.4). In this configuration the detector is placed as close as physically possible to the vacuum-air barrier for minimization of beam broadening and beam scattering. The slot for the detector is slightly deeper than the detector so that a sample can be secured directly above it while not touching the detector. This is important so that no unintended electrical connections are made to the detector. Lastly, the square holes in the mount are for easy installation and removal of the detector.

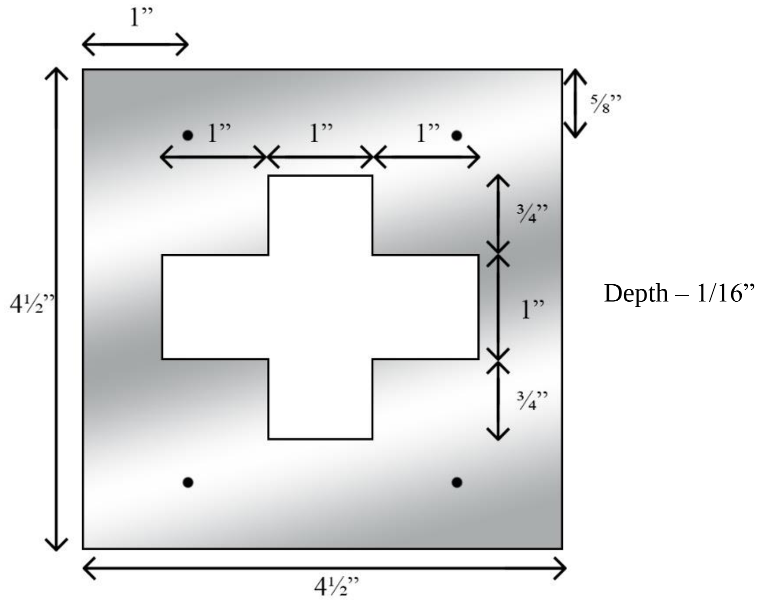

Figure 2.3: Diagram of new detector and sample mount. Black dots represent holes for 4-40 screws.

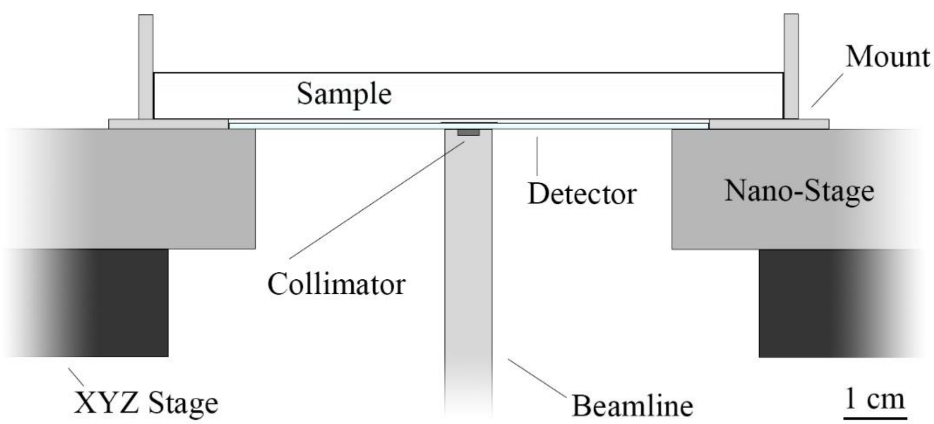

Figure 2.4: Placement of new detector, detector mount and sample within the microbeam end-station. Dimensions are to scale.

2.7 Experimental Setup

Once both detectors were constructed, they were inserted into the detector mount and connected to a Canberra Model 2006 preamplifier. The voltage was supplied by a Canberra Model 3125 Dual High Voltage Power Source for initial experiments but was replaced by a Hamamatsu Model C9525 High Voltage Power Supply for its better voltage control. The signal was passed through a Canberra Model 2022 amplifier and finally into a Fluke 199C Scopemeter Color oscilloscope. A schematic of the electronics system is summarized in Figure 2.5.

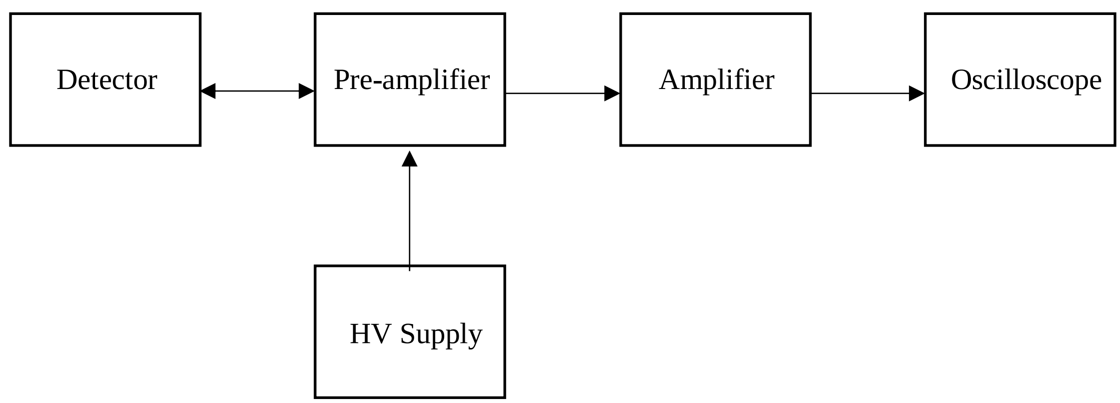

Figure 2.5: Schematic of detector electronics setup.

2.8 I-V Curve

Negative voltages were supplied by a CAEN DT5534EM HV supply while the currents were monitored with CAEN Geco 2020 Software. Positive voltages were supplied by a Keithley 2260B-80-13 HV supply with those currents being monitored with a multimeter. Only the second constructed detector had its I-V curve measured.

2.9 ^{244}Cm Alpha Source Experiments

For alpha source experiments, the high voltage bias was set to 40 V and a 3.699 kBq ^{244}Cm source (5.81 MeV alpha emitter, decayed to 2.705 kBq by April 2017) was positioned 2 cm away from the bottom of the detector. In one experiment the voltage was increased from 0 V to 700 V in increments of 10 V. The range of 5.81 MeV alpha particles in air is 4.5 cm[26].

Theoretically, semiconductors can operate as detectors without any bias, albeit poorly. In an experiment to compare the bias dependence on detector signal, the curium source was placed in front of a 500 μm silicon Ortec detector. The signal was observed over the bias range of 0 V to 100 V.

2.10 TRIM Simulations

TRIM was used as a simple way to obtain an idea of how the protons would scatter through the various materials in the detection setup. All of the TRIM simulations completed had geometries shown in Figure 2.6 including a 2 μm Mylar window, an air gap of varying length and pressure, a varying thickness of silicon, and finally another varying air layer. Information about each proton reaching the far side of the second air layer is saved to an output file, including proton energy and position. Using Excel, histograms of the proton positions were created to quantitatively assess proton distribution at the sample surface. Each run consisted of 50,000 protons.

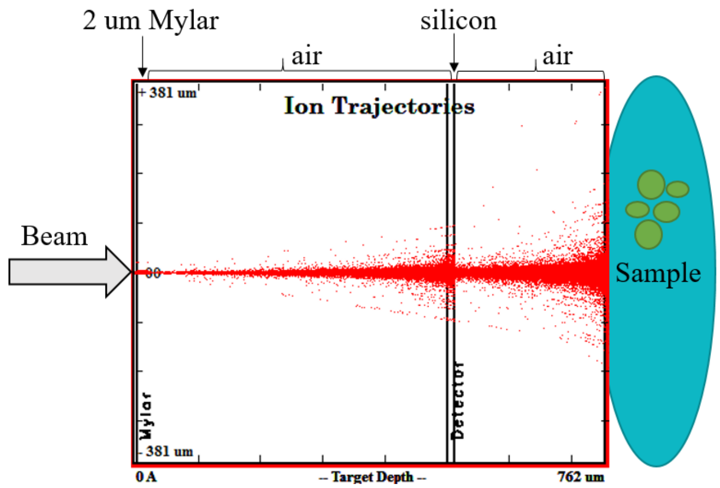

Figure 2.6: Annotated TRIM ion trajectory plot. Red dots represent interaction events.

To mitigate the point source limitation of TRIM, twenty simulations were computed with varying source angles within the exit angle of the 5 ± 1 μm diameter collimator. These simulations were computed using the minimum air thicknesses thought to be reasonably achievable. The gap before the detector was set to 0.5 mm, the thickness of the glass slide the detector was to be mounted on. The gap after the detector was set to 0.25 mm, to just enough room for the microwires attached to the detector electrodes. The outputs were summed together and a histogram was then generated. This process was done twice, once for a uniform distribution of source angles and once for a Gaussian distribution.

2.11 MCNP Simulations

MCNP was used to verify the validity of the TRIM approximations and to provide a more accurate calculation of beam broadening. The FS2 tally was chosen to indirectly compute proton distributions for its simple implementation. Afterwards, the number of protons hitting each segment from the tally can be found by simply multiplying the fluence for that segment by the area of that segment. Figure 2.7 shows the segment geometry used in all computations.

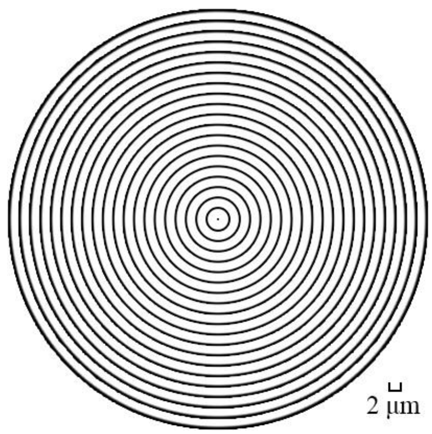

Figure 2.7: Segmentation of sample surface for average fluence computation in MCNP.

Three simulations with different geometries were completed with one million protons each. The first geometry was analogous to that of the TRIM computations utilizing a monodirectional point source. The second replaced the point source with a uniform disc source, and the third incorporated the geometry of the double aperture collimator along with the same disc source.

3. Results & Discussion

3.1 Collimator

The final spacer length for the new double aperture collimators was chosen to be 925 microns. At that region in the exit angle plot (Figure 1.5) the curve flattens out considerably and so a marked increase in spacer length would be required to further reduce the collimator exit angle. The spacer length could be increased even multiple orders of magnitude before the proton exit rate was too small for reasonable experiment times (Figure 1.6). However, the limit to the length is the existing collimator mount, which can only accommodate a collimator up to a few millimeters. The solid angles and beam broadening corresponding to new collimators manufactured at this length (Lenox Laser, Glen Arm, USA) are summarized in Figure 1.4.

3.2 Monte Carlo Simulations

3.2.1 TRIM Simulations

One valuable feature of TRIM is as simulations run, a plot of particle tracks is generated in real-time. This allows for qualitative assessment of geometry effectiveness even before simulations are completed. This saved time in the early stages of parameter optimization. For example, it was observed that changing the pressure of the air layers both before and after the detector had little impact on beam scattering, in the range of 1 μTorr to atmospheric pressure. This is because scattering from the detector was significantly more influential. Additionally it was observed that changing the detector to sample distance was much more impactful on beam scattering than the vacuum-air barrier to detector distance. This is again due to the scattering through the detector being the primary source of beam scattering.

The results of the summed simulations as compared to the analogous point source are summarized in Table 3.1 and Figure 3.1. In both cases the goal of 95% of protons hitting within a 20 μm radius is met. It was expected that the uniform angular distribution would even be a conservative estimate for proton scattering and so the detection system dimensions used in this experiment were deemed acceptable to use as the basis for beginning construction.

Table 3.1: Comparison of TRIM proton distributions at target.

Distance from beam center	Point Source	Gaussian Angles	Uniform Angles
≤ 10 μm	94.5 %	92.6 %	87.5 %
≤ 20 μm	99.0 %	98.9 %	98.7 %

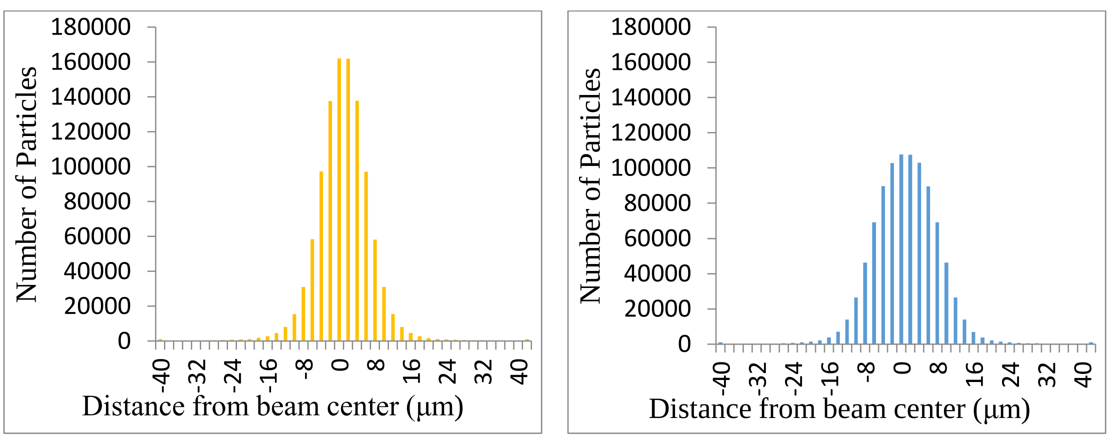

Figure 3.1: Histograms of TRIM proton positional distributions at sample from summed Gaussian (left) and uniform (right) angular distributions.

3.2.2 MCNP Simulations

The first geometry set up was meant to mimic the TRIM simulations, using a monodirectional point source and no consideration for collimator geometry yet. The results, outlined in Table 3.2 and Figure 3.2 show a difference in proton distribution at the sample. The TRIM distribution has a clear maximum in the center of the beam which tapers off with increasing distance. Conversely, the MCNP distribution shows a maximum hit density around 6 μm. The MCNP results make sense because even though the fluence may be the highest in the beam center, the area of the innermost segments are very small so there are fewer particles hitting.

Table 3.2: Comparison of TRIM to MCNP proton distributions at target from a point source.

Distance from beam center	TRIM	MCNP
≤ 10 μm	94.5%	74.8%
≤ 20 μm	99.0%	96.9%

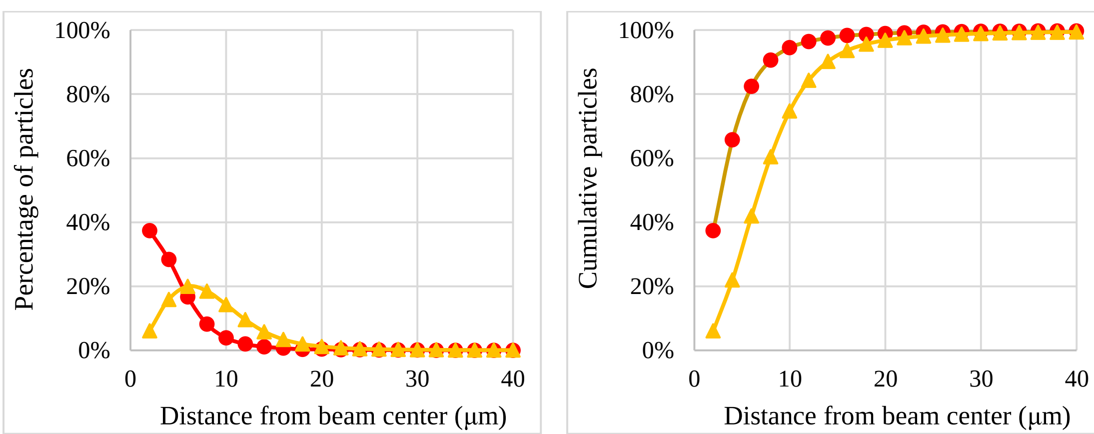

Figure 3.2: Proton distribution comparison of TRIM point source (red circles) to analogous MCNP point source (orange triangles).

The next computation was to compare how the angular distribution summations done in TRIM would compare to a disc source in MCNP. A 5 μm source was utilized since the TRIM distributions were based on the leaving angle of the 5 ± 1 μm diameter collimator aperture. Table 3.3 and Figure 3.3 show the results which show a similar distribution pattern to the plots in the previous section. As expected, the MCNP distribution is broader for the disc source than the point source. However, both are broader than the TRIM results. Before using MCNP, the uniform angular distribution computed in TRIM was thought to have been a conservative estimate for the extent of proton scattering. The geometry of the TRIM model was used for the detector and detector mount construction. However, from the MCNP data it can be seen that the TRIM data underestimated proton scattering.

Table 3.3: Comparison of TRIM proton distributions to a disc source in MCNP at target.

Distance from beam center	TRIM Gaussian	TRIM Uniform	MCNP Disc
≤ 10 μm	92.6%	87.5%	69.3%
≤ 20 μm	98.9%	98.7%	96.4%

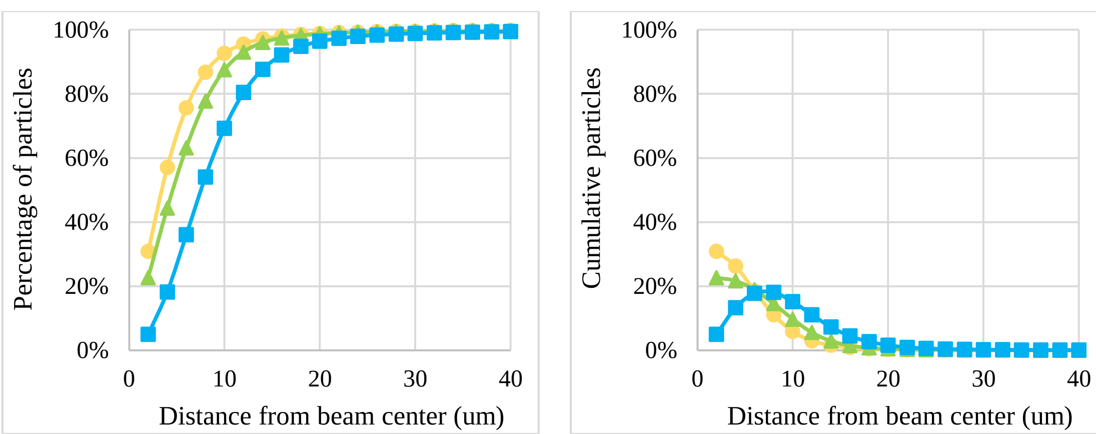

Figure 3.3: Proton distribution comparison of TRIM Gaussian (yellow circles) and uniform (green triangles) angular distribution to a disc source in MCNP (blue squares).

The last MCNP experiment was to model the double aperture collimator and to compare the proton distribution with and without it. A uniformly distributed disc source was also used for this computation, the results are summarized in Table 3.4 and Figure 3.4. Comparing this data to the analogous MCNP simulation without the collimator shows a further increase in distribution and for the first time a result where less than 95% of protons hit within 20 μm of beam center. Since this geometry is truest to an experimental setup, this computation is considered the most accurate for estimating proton distribution at the target.

Table 3.4: Comparison of MCNP proton distributions at target with and without a collimator.

Distance from beam center	No collimator	Collimator
≤ 10 μm	69.3%	57.7%
≤ 20 μm	96.4%	93.2%

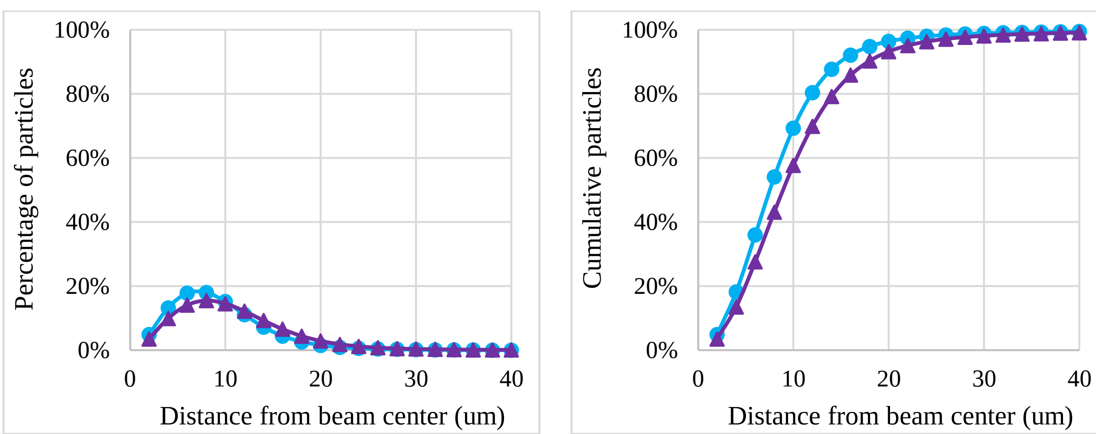

Figure 3.4: MCNP Proton distribution comparison of a disc source without (blue circles) and with a double aperture collimator (purple squares).

3.3 I-V Curve

The most useful experiment to perform first is to test whether the detector functions as a diode. If a negative voltage is applied, no current should be induced, whereas a positive voltage should correspond to a rapidly increasing current. The current-voltage (I-V) curve in Figure 3.5 shows the relationship that is expecting for a rectifying diode. This means that the detector is correctly constructed and wired to work as a Schottky diode.

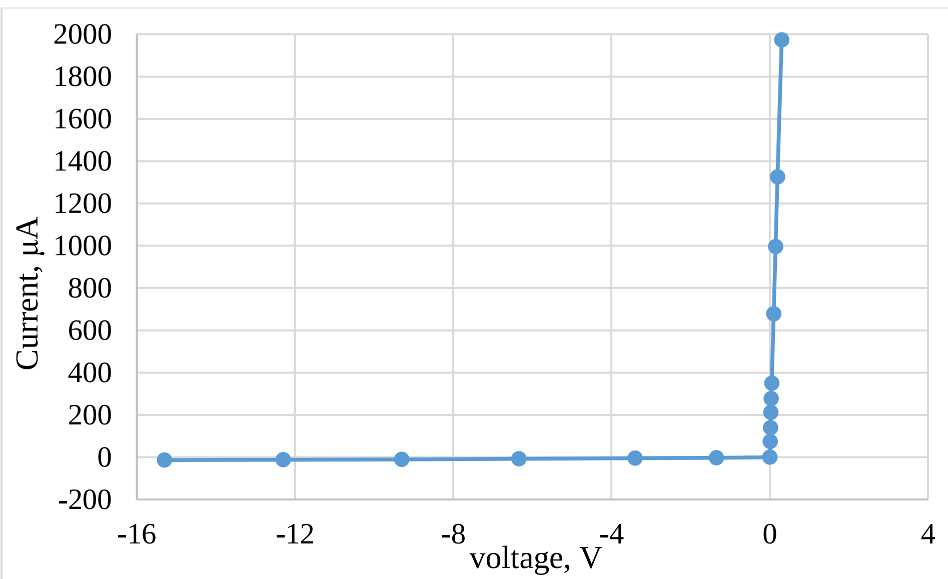

Figure 3.5: Schottky diode detector I-V curve.

3.4 Depletion Depth Curve

The silicon wafer supplier could only provide $\sim 1 - 4 \times 10^{15}\ \frac{atoms}{cm^3}$ as their best estimate of impurity concentration for the wafers that were purchased. Based on this estimate the plot in Figure 3.6 of depletion depth as a function of voltage was created using Equations 1.1 through 1.3. Given the manufacturer uncertainty in both wafer thickness and impurity concentration it was calculated that the bias voltage required for full depletion was in the range of 49 – 446 Volts. When reverse biased, Schottky diodes have large leakage currents that increase with the reverse bias[27,28]. Since the range of possible full depletion voltages is above operating voltages described in literature[17], it is possible that the signal-to-noise ratio is poor enough that a radiation response cannot be distinguished.

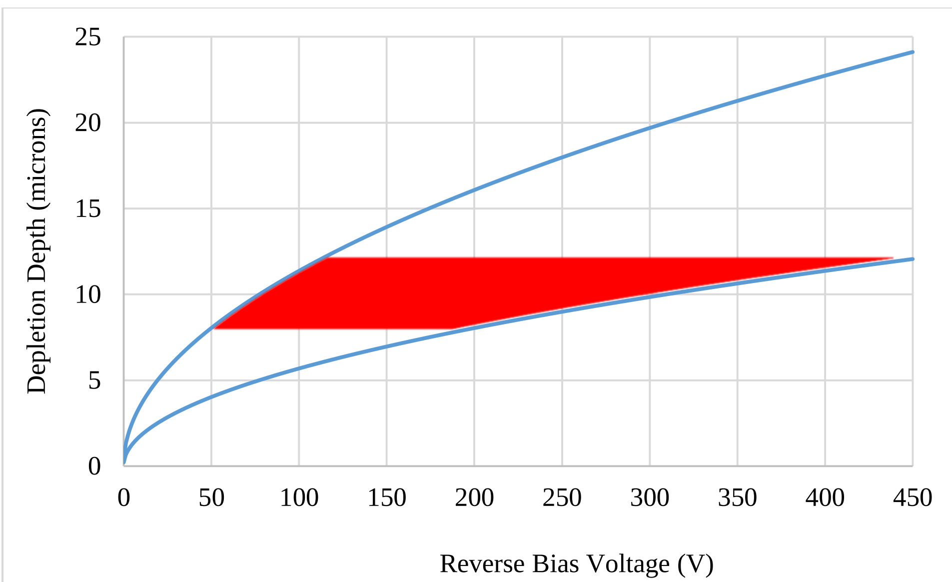

Figure 3.6: Depletion depth curves for silicon-gold junctions with impurity concentrations of $1 \times 10^{15}\ \frac{atoms}{cm^3}$ (top) and $4 \times 10^{15}\ \frac{atoms}{cm^3}$ (bottom). The region in red highlights the purchased wafer thickness.

3.5 ^{244}Cm Alpha Source Experiments

The first detector built showed immediate signs of response to radiation as assessed by an oscilloscope trace. Removing and replacing the source multiple times resulted in the traces shown in Figure 3.7. The images in the figure are of low quality because since that first experiment, response to the source was not observed again by either detector.

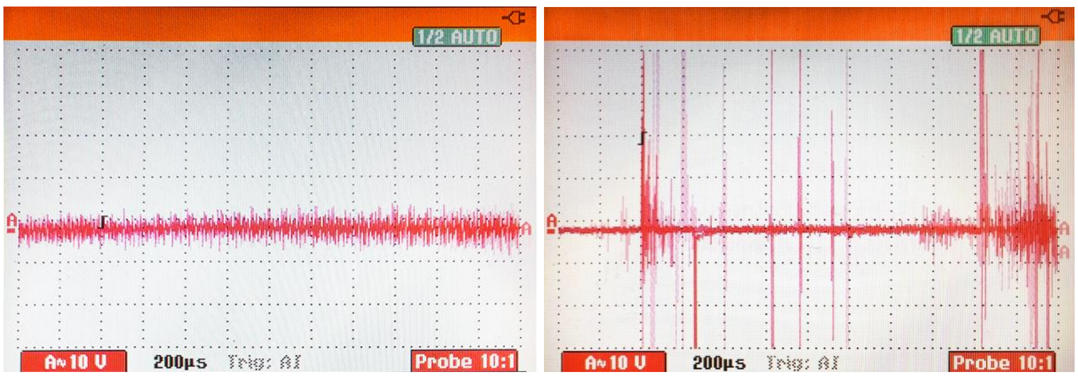

Figure 3.7: Oscilloscope traces of amplifier output, both without the alpha source in front of the detector (left) and with it (right).

Several changes to the electronics setup were done to try to identify the root of the problem. The 10 foot SHV cable connecting the detector and preamplifier was replaced by a 6 inch cable. One of the BNC cables was found to have a high noise level and was replaced. Multiple high voltage supplies, preamplifiers and amplifiers were also tested. The entire detection system was even tested in two different buildings because even though it was connected to an isolation transformer in the McMaster Microbeam Laboratory, the building is on a ground loop with a significant interference signal. According to the depletion depth that was calculated, experiments were conducted from 0 to as high as 700 V but still there was no indication of radiation response.

Using Figure 3.7, a rough count rate can be calculated. Although individual pulses are difficult to distinguish, approximately 10 to 20 pulses can be observed over 2,400 μs, corresponding to a count rate of 4,200 - 8,300 cps. The source activity at the time of the experiments was 2.705 kBq which is 1.5 - 3 times lower than the observed potential count (without consideration of solid angles). This suggests that the observed signal is not a radiation response.

For the experiment with the commercial 500 μm detector, at no bias, a very weak radiation response was observed. This signal increased in amplitude as the bias was increased up to the operating voltage of 100 V. Since the alpha particles would not fully deposit their energy in the 10 μm detectors, an incorrect bias could result in a signal too small to be observed.

4. Future Work

4.1 Lower Doped Silicon

As discussed in section 3.4, the dopant concentration of the silicon used to construct the detectors leads to an operating bias high enough for leakage current to be an issue. Constructing detectors using silicon wafers with a lower dopant concentration would improve signal-to-noise ratios.

4.2 Further Characterization

Once the detectors show a proper response to radiation, it will be useful to complete other standard characterizations for this type of detector. This includes creation of a capacitance-voltage curve, and determination of the Full Width at Half Maximum (FWHM), dead time and leakage current. The detector efficiency can be found by setting up a coincidence counting system with a commercial detector. In this experiment the transmission detector would be placed between the source and commercial detector. Since the range of the source is much less than the thickness of the commercial detector, it would be assumed that all protons would be counted by the commercial detector. The ratio of coincidence counts to total commercial detector counts would be a measurement of the efficiency of the transmission detector.

A commercial detector could also be used to indirectly find the precise transmission detector thickness. This would be useful to know since the silicon wafer manufacturer provides a 20% thickness uncertainty. In such an experiment the commercial detector would measure the energies both with and without the transmission detector situated in front of it. The difference in energy can be related to stopping power to find the silicon thickness.

4.3 Detector Library

The designed transmission detector was optimized to reduce beam scattering of a 3 MeV proton beam, and so it would not be suitable for use with a lower energy beam. It would be of interest for future radiation biology experiments to have more freedom in what proton energies are possible to use. Since the McMaster Microbeam Laboratory can produce proton beams with a maximum energy of 3 MeV protons, only detectors meant for lower energy experiments need to be considered. As proton energy decreases, LET increases and range decreases. Therefore, a transmission detector for lower proton energies would require thinner silicon.

4.4 Biological Experiments

Once detectors are completely characterized and proven to operate with sufficient stability, radiation biology experiments can commence. AGO1522 human fibroblasts have already been selected by collaborating biologists as a candidate for initial proton irradiations.

5. Conclusions

The goal of this project was to design and construct a transmission detector capable of both accurate single proton counting and targeting a spot only 20 μm in radius. Of the detectors reported in literature for the same application, a Schottky diode based design was chosen based on its short construction procedure. Reduction of beam broadening and beam scattering were the biggest design challenges to overcome since they were influenced by several factors. The best design was a very compact one and also required fabrication of new double aperture collimators and a new detector mount. Specialty silicon wafers with a thickness of 10 ± 2 μm were acquired to remove the tedious task of thinning thicker wafers down to that range.

An initial experiment using the first fully constructed detector with an alpha source showed promising radiation response. However, this response was not able to be observed again. A second detector was constructed and its current-voltage curve obtained which proved that it functioned correctly as a diode. However, multiple experiments with an alpha source to prove that it could function as a radiation detector were unsuccessful.

Future work foremost involves investigation to understand the lack of radiation response. One avenue worth exploring is acquiring thin silicon of a lower dopant concentration. Afterwards, a full electrical characterization of the detectors is necessary before the detectors can be used as intended in microbeam assisted radiation biology experiments. Constructing Schottky diodes using diamond membranes instead of silicon is an intriguing option for further improving targeting abilities.

6. References

1. Zirkle RE, Bloom W. Irradiation of parts of individual cells. Science. 1953; 117(80):487-493.

2. Prise KM, Schettino G. Microbeams in Radiation Biology: Review and Critical Comparison. Radiation Protection Dosimetry. 2011; 143(2-4):335-339.

3. Grilj V, Skukan N, Pomorski M, Kada W, Iwamoto N, Kamiya T, Ohshima T, Jaksic M. An ultra-thin diamond membrane as a transmission particle detector and vacuum window for external microbeams. Applied Physics Letters. 2013; 103:243106.

4. Buonanno M, Randers-Pehrson G, Smilenov LB, Kleiman NJ, Young E, Ponnayia B, Brenner DJ. A Mouse Ear Model for Bystander Studies Induced by Microbeam Irradiation. Radiation Research. 2015; 184:219-225.

5. Knoll, GF. Radiation Detection and Measurement Third Edition. Chapter 11: Semiconductor Diode Detectors. John Wiley & Sons. 1999.

6. Van Zeghbroeck, B. Principles of Semiconductor Devices. Chapter 3: Metal-Semiconductor Junctions. 2011.

7. Garty G, Ehsan MU, Buonanno M, Yang Z, Sweedler JV, Brenner DJ. Microbeam-Coupled Capillary Electrophoresis. Radiation Protection Dosimetry. 2015; 166(1-4):188-191.

8. Fischer BE. Ion-Microbeams and Their Role in Radiobiology in Europe. GSI Biophysics. 2011.

9. Folkard M, Vojnovic B, Schettino G, Forsberg M, Bowey G, Prise KM, Michael BD, Michette AG, Pfauntsch SJ. Two approaches for irradiating cells individually: a charged-particle microgram and a soft X-ray microprobe. Nucl. Instrum. Methods Phys. Res. B. 1997; 130:270-274.

10. Moretto P, Michelet C, Balana A, Barbaret P, Przybylowicz WJ, Slabbert JP, Prozesky VM, Pineda CA, Brut G, Laurent G, Lhoste F. Development of a single ion irradiation system at CENBG for applications in radiation biology. Nucl. Instrum. Methods. Phys. Res. B. 2001; 181:104-109.

11. Nilsson C, Pallon J, Thungstrom G, Marrero NA, Elfman M, Kristiansson P, Nilsson C, Wegden M. Characterisation of a pre-cell hit detector to be used in single cell irradiation experiments at the Lund Nuclear Microprobe. Nuclear Instruments and Methods in Physics Research Section B: Beam Interactions with Materials and Atoms. 2008; 266(21):4808-4815.

12. Ortec. *Silicon Charged Particle Radiation Detectors: D Series*. Oak Ridge, TN: Ortec, 2015. Online.

13. Nilsson C, Pallon J, Thungstrom G, Arteaga N, Auzelyte V, Elfman M, Kristiansson P, Nilsson C, Wegden M. Evaluation of a pre-cell hit detector for the future single ion hit facility in Lund. Nuclear Instruments and Methods in Physics Research Section B: Beam Interactions with Materials and Atoms. 2006; 249(1-2):924-927.

14. Thungstrom G, Westerberg L, Spohr R, Petersson CS. Fabrication and characterization of thin ΔE detectors for spectroscopic application. Nuclear Instruments and Methods in Physics Research Section A: Accelerators, Spectrometers, Detectors and Associated Equipment. 2005; 546:312-318.

15. Abdel NS, Pallon J, Ros M, Borysiuk M, Elfman M, Kristiansson P, Nilsson CEJ. Characterizations of new ΔE detectors for single-ion hit facility. Nuclear Instruments and Methods in Physics Research Section B: Beam Interactions with Materials and Atoms. 2014; 318:281-286.

16. Abdel N, Pallon J, Graczyk M, Maximov I, Wallman L. Fabrication and Characterization of Ultra-Thin PIN Silicon Detectors for Counting the Passage of MeV Ions. IEEE Transactions on Nuclear Science. 2013; 60(2):1182-1188.

17. Grad M, Harken A, Randers-Pehrson G, Attinger D, Brenner DJ. An ultra-thin Schottky diode as a transmission particle detector for biological microbeams. Journal of Instrumentation. 2013;7:P12001.

18. Pomorski M, Caylar B, Bergonzo P. Super-thin single crystal diamond membrane radiation detectors. Applied Physics Letters. 2013; 103:112106.

19. Abdel NS, Pallon J, Elfman M, Kristiansson P, Nilsson CEJ, Ros L. Radiation tolerance of ultra-thin PIN silicon detectors evaluated with a MeV proton microbeam. Nuclear Instruments and Methods in Physics Research Section B: Beam Interactions with Materials and Atoms. 2015; 356-357:17-21.

20. Vander AJ, Sherman JH, Luciano DS. Human Physiology: The Mechanisms of Body Function, Fifth Edition. McGraw-Hill Publishing Company, New York. 1990.

21. Levina EM, Kharitonova MA, Rovensky YA, Vasiliev JM. Cytoskeletal control of fibroblast length: experiments with linear strips of substrate. Journal of Cell Science. 2001; 114:4335-4341.

22. Gerardi, S. A Comparative Review of Charged Particle Microbeam Facilities. Radiation Protection Dosimetry. 2007; 122 (1-4):285-291.

23. National Institute of Standards and Technology – Physical Meas. Laboratory. Stopping-Power and Range Tables for Protons. Retrieved from physics.nist.gov/PhysRefData/Star/Text/PSTAR.html.

24. Sayah R, Donadille L, Aube A, Herault J, Delacroix S, De Marzi L, Stichelbaut F, Clairand I. Monte Carlo simulation of a proton therapy beamline for intercranial treatments. Radioprotection. 2013; 48 (3):317-339.

25. Ziegler JF, Biersack JP, Ziegler MD. SRIM The Stopping and Range of Ions in Matter. Lulu Press Company, Morrisville. 2008.

26. National Institute of Standards and Technology – Physical Meas. Laboratory. Stopping-Power and Range Tables for Alpha Particles. Retrieved from physics.nist.gov/PhysRefData/Star/Text/ASTAR.html.

27. Colinge JP, Colinge CA. Physics of Semiconductor Devices. Kluwer Academic Publishers, New York City. 2005

28. Sze SM. Physics of Semiconductor Devices. John Wiley & Sons, New York. 1969.